

## A Numerical Study of the Evolving Convective Boundary Layer and Orographic Circulation around the Santa Catalina Mountains in Arizona. Part II: Interaction with Deep Convection

J. CORY DEMKO AND BART GEERTS

*University of Wyoming, Laramie, Wyoming*

(Manuscript received 14 December 2009, in final form 7 April 2010)

### ABSTRACT

This is the second part of a study that examines the daytime evolution of the thermally forced boundary layer (BL) circulation over a relatively isolated mountain, about 30 km in diameter and 2 km high, and its interaction with locally initiated deep convection by means of numerical simulations validated with data collected in the 2006 Cumulus Photogrammetric, In Situ, and Doppler Observations (CuPIDO) field campaign in southeastern Arizona. Part I examined the BL circulation in cases with, at most, rather shallow orographic cumulus (Cu) convection; the present part addresses deep convection. The results are based on output from version 3 of the Weather Research and Forecasting model run at a horizontal resolution of 1 km. The model output verifies well against CuPIDO observations.

In the absence of Cu convection, the thermally forced (solenoidal) circulation is largely contained within the BL over the mountain. Thunderstorm development deepens this BL circulation with inflow over the depth of the BL and outflow in the free troposphere aloft. Primary deep convection results from destabilization over elevated terrain and tends to be triggered along a convergence line, which arises from the solenoidal circulation but may drift downwind of the terrain crest. While the solenoidal anabatic flow converges moisture over the mountain, it also cools the air. Thus, a period of suppressed anabatic flow following a convective episode, at a time when surface heating is still intense, can trigger new and possibly deeper convection. The growth of deep convection may require enhanced convergent flow in the BL, but this is less apparent in the mountain-scale surface flow signal than the decay of orographic convection. A budget study over the mountain suggests that the precipitation efficiency of the afternoon convection is quite low,  $\sim 10\%$  in this case.

### 1. Introduction

This is the second part of a two-part paper that examines the daytime evolution of the thermally forced boundary layer (BL) circulation over an isolated mountain, about 30 km in diameter and 2 km high, and the interaction of this circulation with orographic cumulus (Cu) convection. In Demko and Geerts (2010, hereafter Part I), two cases were presented: one was cloud free and the second produced orographic convection just deep enough to yield a trace of precipitation. In the present study, a third case is analyzed, in which isolated, deep, precipitating convection developed over the mountain.

Most of the warm-season precipitation in arid mountainous regions results from deep convection that is triggered over the mountains (e.g., Banta and Schaaf 1987;

Gochis et al. 2004). This study is motivated by the importance of this deep convection to warm-season precipitation and the importance of mountains as a conduit of surface–BL–troposphere exchanges of water and heat. Because the BL depth and circulations in complex terrain are inadequately represented by numerical weather prediction (NWP) models, the predictability of this precipitation is relatively poor (e.g., Giorgi 1991; Bright and Mullen 2002). The poor predictability is only in part due to the small size of the mountains over which thunderstorms form, compared to the resolution of current-generation NWP models (e.g., Yuan et al. 2007). Yet even NWP model simulations of sufficient resolution to resolve the thermally direct orographic circulations are challenged in their ability to simulate the surface fluxes and convective BL (CBL) growth over complex terrain and thus to accurately predict the timing and intensity of the first orographic thunderstorms (e.g., Walser and Schär 2004; Li et al. 2004; Hohenegger and Schär 2007). Such accurate prediction is important because the energy

---

*Corresponding author address:* Bart Geerts, Department of Atmospheric Sciences, University of Wyoming, Laramie, WY 82071.  
E-mail: geerts@uwyo.edu

released in a thunderstorm is far greater than that associated with the orographic BL circulation, and thus primary convective initiation drives subsequent deep convection, including mesoscale convective systems (e.g., Wandishin et al. 2008), which may develop in the evening during the Arizona monsoon (e.g., McCollum et al. 1995; Damiani et al. 2008).

This study focuses on the Santa Catalina Mountains (CM) in Arizona, the target area of the Cumulus Photogrammetric, In Situ, and Doppler Observations (CuPIDO) experiment in July and August 2006 (Damiani et al. 2008). On most days during CuPIDO a deep, weakly capped CBL developed, and tropospheric winds were weak. This study mainly employs output from version 3 of the Weather Research and Forecasting (WRF) model (Skamarock et al. 2008). The simulations compare favorably with CuPIDO observations for the two case studies in Part I.

This modeling study builds on an observational study (Demko et al. 2009) that uses CuPIDO data in order to document a toroidal heat island circulation within the CBL, centered at the mountain. Data from 10 surface stations, positioned around the mountain, clearly demonstrate the diurnal cycle of mountain-scale convergence (MSC), peaking close to local solar noon. On days without deep convection, the daytime evolution of this surface MSC is rather unperturbed and is in sync with the anabatic horizontal pressure gradient force (Geerts et al. 2008). On days with deep convection in the afternoon, the surface flow around the CM tends to temporarily become divergent following a convective outbreak, due to cold-pool spreading (Geerts et al. 2008; Demko et al. 2009). Yet CuPIDO observations do not clearly reveal the solenoidal *forcing* (i.e., a warm anomaly in the CBL over the mountain) or the full solenoidal circulation (with divergent flow near the CBL top). Moreover, observations fail to capture any enhanced MSC near the surface preceding vertical growth spurts of orographic convection (Demko et al. 2009).

The WRF simulations for the two cases presented in Part I do reveal a warm anomaly over the high terrain during the day. On both days this anomaly is rather shallow and does not extend over the depth of the CBL, which bulges over the mountain. They also reveal a solenoidal circulation with divergent flow mostly contained within the CBL, but even in the model output this circulation and especially its upper-level return flow branch are difficult to capture, since they are overwhelmed by thermals. Regarding the effect of moist convection, the simulations for the second case in Part I show that relatively shallow cumulus convection can temporarily overwhelm surface MSC by cloud shading and convective downdraft dynamics.

The objective of Part II is to use the dynamically consistent, continuous WRF model output for a CuPIDO case to shed light upon how the convergent BL circulation affects the initiation and evolution of orographic thunderstorms, and how deep convection affects the BL circulation. The same analysis method as in Part I is used, and a distinction will be made between an early period with mediocre convection and a later period with cumulonimbus development. The horizontal and vertical fluxes of mass, sensible heat, and vapor in/out of the CBL and free troposphere over the mountain will be examined and contrasted with the dry case in Part I.

The remainder of this paper is organized as follows: section 2 compares the WRF simulated with the observed evolution of the CBL circulation and convection for this CuPIDO case. Section 3 uses model output to examine the interaction between CBL circulation and deep convection. The budgets of mass, heat, and moisture over the mountain are discussed in section 4. Section 5 discusses the key results and section 6 lists the conclusions.

## 2. Model validation

This paper focuses on daytime convective development on 6 August 2006, which was chosen for several reasons. First, isolated orographic cumulus grew into cumulonimbus clouds over the CM without much interaction with convection developing over mountains in the vicinity. Second, the deep-layer mean wind ( $3 \text{ m s}^{-1}$  from the east) and wind shear were relatively weak. And third, the convective available potential energy (CAPE) was relatively low, such that deep convection remained mostly confined to the mountains. In several other CuPIDO cases, deep convection broke out over the mountain and soon thereafter over the surrounding valleys, such that it became impossible to discern the orographic BL circulation.

The WRF Nonhydrostatic Mesoscale Model (WRF-NMM), version 3.0.1.1, is used, with initial and boundary conditions determined by the 12-km North American Mesoscale (NAM) grids. The model is initialized at 0000 UTC (i.e., the evening before), and the model forecast for 6–30 h is analyzed. Three nested domains are used (Fig. 1 in Part I), with two-way interaction between domains. Cumulus convection is resolved in the mid and inner domains. Here we only examine output from the inner domain,  $103 \times 103 \text{ km}^2$  with a resolution of 1.0 km. The simulations analyzed here use the Mellor–Yamada–Janjić planetary boundary layer (PBL) scheme (Janjić 1996) with an Eta similarity parameterization for the surface layer, the Noah land surface model (Ek et al. 2003), and the Lin et al. (1983) bulk microphysics scheme. The model output

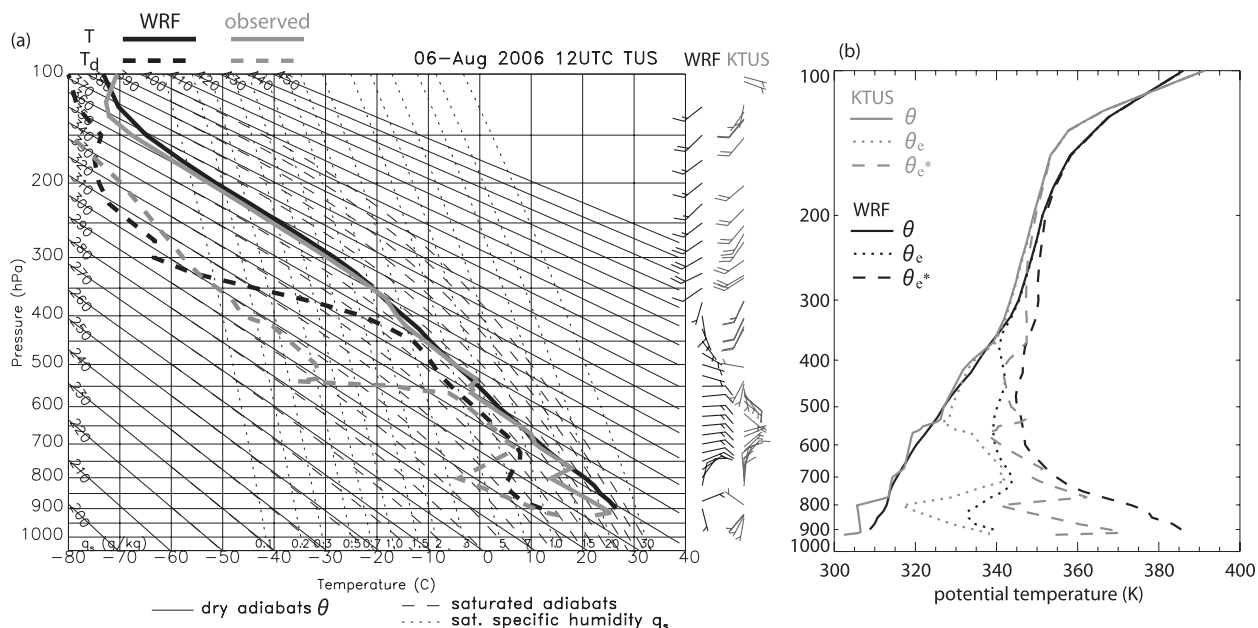


FIG. 1. (a) Tucson (KTUS) 1200 UTC 6 Aug 2006 observed (gray lines and symbols) and model (black) soundings on a Stüve diagram, with wind profiles on the right. A full barb corresponds with  $5 \text{ m s}^{-1}$  (10 kt), and no wind symbol is shown for winds weaker than  $1.3 \text{ m s}^{-1}$ . (b) Corresponding profiles of potential temperature  $\theta$ , equivalent potential temperature  $\theta_e$ , and saturated equivalent potential temperature  $\theta_e^*$ . KTUS is located 38 km from Mt. Lemmon, to the south.

includes a variable called PBL depth, which is displayed in several figures below. For more information about numerical model setup and sensitivity tests, the reader is referred to Part I.

*a. Sounding data and cumulus evolution*

The Tucson, Arizona (KTUS), 1200 UTC (predawn) sounding reveals several stable layers below 500 hPa, with the strongest ones around 780 hPa, or slightly below the level of Mt. Lemmon [the peak of the CM at an elevation of 2791 m ( $\sim 730$  hPa)] and around 550 hPa (Fig. 1a). Predawn winds were very weak ( $<5$  kt) below mountain top level; weak easterly flow was present between 700 and 600 hPa, and stronger southwesterly flow above 450 hPa, up to the tropopause. Weak winds persisted during the day (Fig. 2), mostly  $<10$  kt (south)easterly winds below 400 hPa and slightly stronger ( $<15$  kt) southwesterly winds above 400 hPa, according to the four Mobile GPS Advanced Upper-Air Soundings (MGAUS) collected on 6 August. The MGAUS sondes were released from Stratton Canyon located 12 km east-northeast of Mt. Lemmon (Fig. 3). The location was selected because the mean wind in the cumulus layer was expected to carry convection to the west, which it did. So the MGAUS profiles represent conditions close to the mountain, but hardly affected by orographic convection.

The 1200 UTC WRF sounding at the location of KTUS does not reveal the multiple low-level stable

layers and it overestimates the 700–600-hPa easterly jet (Fig. 1). By the time of first cumulus convection over the CM, the model profiles are closer to the observed (MGAUS) profiles (Fig. 2). The model nicely captures the upstream wind profile during the period of convective growth (1800–2100 UTC). It underestimates the BL temperature at 1931 UTC (local solar noon) but overestimates it at 2100 UTC (Fig. 2). The BL water vapor mixing ratio was estimated accurately at 1752 UTC, but underestimated in the model by  $2\text{--}3 \text{ g kg}^{-1}$  at 1931 and 2100 UTC. Apparently humidity increased in Stratton Canyon between the three MGAUS sounding times. This is confirmed by data from an Integrated Surface Flux Facility (ISFF) in the canyon. Much of this humidity increase appears to be due to high local evaporation from a nearly saturated soil (not shown). WRF also increases the surface (2 m) mixing ratio, mainly on the northern periphery of the mountain (as observed), but less rapidly and  $\sim 2$  h earlier than observed. Stratton Canyon had received much precipitation in previous days. This precipitation was highly heterogeneous in coverage. All nine other ISFF stations around the mountain reported a lower mixing ratio between 1800 and 2300 UTC than at Stratton Canyon, up to  $7 \text{ g kg}^{-1}$  lower. Thus, the MGAUS soundings may overestimate the BL moisture over the CM and the WRF soundings in fact may be more representative. As a result, the observed convection topped well below the equilibrium level (EL)

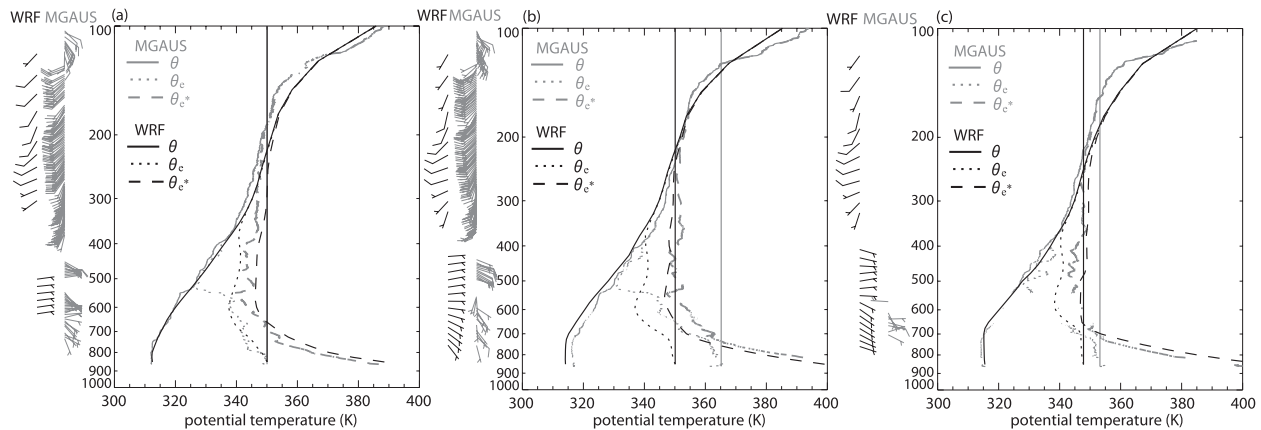


FIG. 2. As Fig. 1b, but the observations (gray) are MGAUSs at (a) 1752, (b) 1931, and (c) 2100 UTC released from Stratton Canyon, located 12 km ENE of Mt. Lemmon. These are compared with collocated WRF soundings at the closest hour (in black). The vertical line carries  $\theta_e$  from the most unstable level near the surface upward, indicating the amount of CAPE in the environment.

in the last three MGAUS soundings. For instance, the 1931 UTC sounding has an EL of 16.5 km (Fig. 2b), whereas the highest cumulus cloud top observed on this day merely reached 9.4 km MSL (Fig. 4a). The MGAUS CAPE values<sup>1</sup> are 2–3 higher than CAPE values in the corresponding WRF soundings (Fig. 4a). Note that WRF uses the Noah land surface model with initial soil moisture provided by the 12-km NAM model.

The model overestimates the humidity above 550 hPa at all times, and it misses a persistent stable layer around 540 hPa (Fig. 2). Both the stable layer and low humidity aloft probably can be attributed to subsidence, which the model apparently fails to capture. This may be one reason why cumulus convection over the CM grows deeper in the model than in reality (Fig. 4a). Another reason why the modeled convection reaches heights closer to the model EL is that the erosive effect of entrainment is captured inadequately in the 1-km simulation. A sensitivity run with an inner domain at 0.5-km horizontal resolution and twice as many levels in the vertical decreases the maximum cloud top at all times (except at the earliest time, 1800 UTC), by 0.8 km on average, but otherwise shows a similar convective evolution compared to the control run. The cloud-top evolution shown in Fig. 4a is inferred from stereo photogrammetry (Zehnder et al. 2007), using two cameras located some 40 km southwest of Mt. Lemmon (Damiani et al. 2008).

<sup>1</sup> The computation of the observed CAPE and CIN required some interpolation because there were gaps in the MGAUS data, as can be seen in Fig. 2. CAPE was computed from the MGAUS and model profiles assuming a 50-mb-deep mixed boundary layer. This computation includes the virtual temperature correction. The model stability parameters were computed for each grid point in the  $30 \times 30 \text{ km}^2$  box shown in Fig. 3 and then averaged.

Cumulus clouds first appeared over the CM at 1840 UTC. They quickly grew to become Cu congestus; a maximum cloud top of 9.4 km MSL was reached at 2100 UTC (Fig. 4a). No lightning was recorded over the CM. The 1931 and 2100 UTC MGAUS soundings reveal virtually no convective inhibition (CIN), although in areas away from Stratton Canyon and the CM there probably was some CIN, as suggested by the lack of convection in the San Pedro and Tucson valleys (Fig. 3). The first orographic Cu developed over the highest ridges (Fig. 4b). Later the deepest convection occurred farther upstream, near the eastern fringes of the CM. Camera animations show that individual cumulus clouds over the CM hardly drifted. Initially clouds slowly moved westward; after 2200 UTC they drifted eastward. Although no precipitation was recorded at any of the ISFF stations or at Mt. Bigelow station, at nearly the same elevation as Mt. Lemmon (locations shown in Fig. 3), the camera footage reveals virga down to the mountain surface—mainly at 2100 UTC.

The model generates some CAPE over the CM, beginning at 1600 UTC and increasing to nearly  $400 \text{ J kg}^{-1}$  3 h later (Fig. 4a). Model CAPE decreases between 1900 and 2100 UTC as nonprecipitating convection develops and then increases again to  $\sim 500 \text{ J kg}^{-1}$ . This value is small compared to typical CAPE values near air mass thunderstorm, but the  $30 \times 30 \text{ km}^2$  box-average CAPE values underestimate model CAPE values closer to Mt. Lemmon. Without substantial CIN, these CAPE values appear to suffice for deep, precipitating convection (topping at 11 km MSL) to develop around 2300 UTC (Fig. 4b).

#### b. Surface measurements

The diurnal surface temperature trend observed at the 10 ISFF stations located in the foothills around the

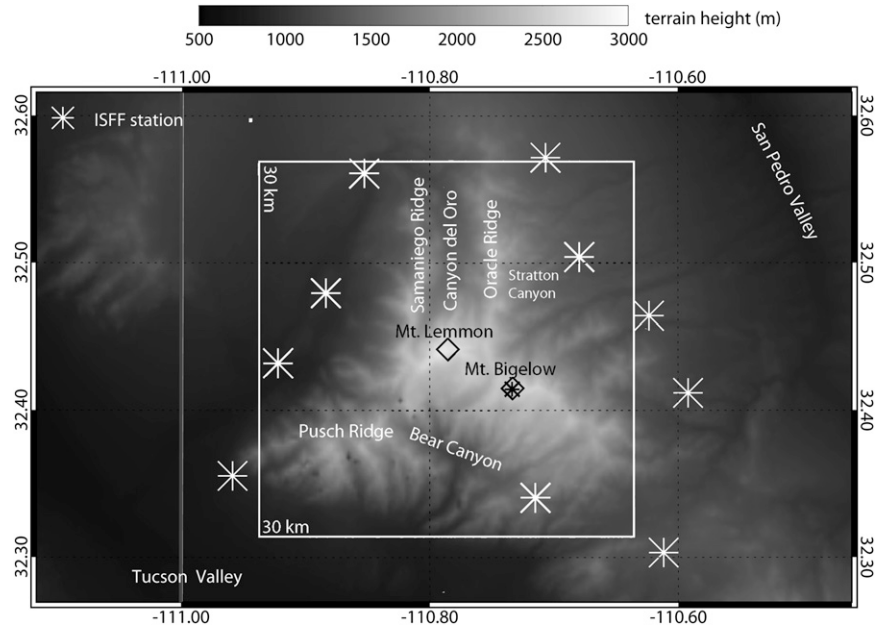


FIG. 3. Terrain map of the Santa Catalina Mountains showing the location of the 10 ISFF stations, the Mt. Bigelow station, the  $30 \times 30 \text{ km}^2$  box used for MSC calculations, and several geographic markers.

mountain is captured rather well by WRF. The main exception is an unobserved, short-lived  $\sim 5\text{-K}$  cooling in most quadrants around the mountain stations at 2300–0000 UTC (Figs. 5a,b), as deep convection matures over the CM in the model (Fig. 4), resulting in a cold pool with divergent surface flow around the mountain (Fig. 5c). The model PBL top is above the CM top for much of the day (1800–2300 UTC; Fig. 4a). The modeled excess potential temperature at Mt. Bigelow over the foothill stations during this period (Fig. 5b) is indicative of solenoidal forcing for a toroidal BL circulation centered over the CM. The observed potential temperature excess at Mt. Bigelow between 1800 and 2300 UTC is smaller. This may be due to cloud shading and cold pool dynamics from orographic cumuli, which peaked earlier (between 2000 and 2200 UTC) than in the model (Fig. 4a).

The surface component of the solenoidal flow is best estimated in terms of MSC (Demko et al. 2009). The MSC shown in Fig. 5c is calculated as the line integral of the surface wind normal to a closed loop around the CM, divided by the area contained within the loop. In the case of ISFF measurements, the loop is a  $576 \text{ km}^2$  decagon (Demko et al. 2009). For validation purposes we mine model output for the same decagon (Fig. 5c). Further model output analysis in this paper uses a more rigorous estimate of MSC, based on a  $30 \times 30 \text{ km}^2$  box centered on Mt. Lemmon (Fig. 3), with 120 points (since the model resolution is 1 km) versus 10 data points (i.e., 10 stations). The MSC within this square is also shown in Fig. 5c.

The modeled nocturnal surface katabatic flow is stronger than observed, but the magnitude of the modeled daytime 10-point MSC matches observations, with net convergence starting between 1400 and 1500 UTC, as observed. The period of convective deepening (2200–2300 UTC, Fig. 4a) corresponds with enhanced surface MSC in the model (Fig. 5c). In reality the deepest convection occurred earlier (Fig. 4a) and its decay is evident in weak mountain-scale surface divergence around 2200 UTC (Fig. 5c).

In addition to surface potential temperature and MSC, we evaluate the horizontal pressure difference between any of the 10 ISFF stations and the mountain top (Figs. 5d,e). This pressure difference is based on the station pressure data, with the 24-h mean at any station and the residual 11-station mean at any given time removed. It also includes a correction for the diurnal temperature and pressure cycles following Geerts et al. (2008). Observations (Geerts et al. 2008) and WRF simulations for two dry cases (Part I) indicate that the horizontal pressure difference typically is negative at night, peaking near sunrise, and typically becomes positive (implying anabatic wind forcing) a few hours after sunrise, peaking in the early afternoon. The 6 August model horizontal pressure difference follows this trend and becomes positive in the morning about 1 h earlier than observed (Figs. 5d,e). Its afternoon maximum is close to the observed value, suggesting that WRF accurately captures the lower-tropospheric temperature variation around the CM (since

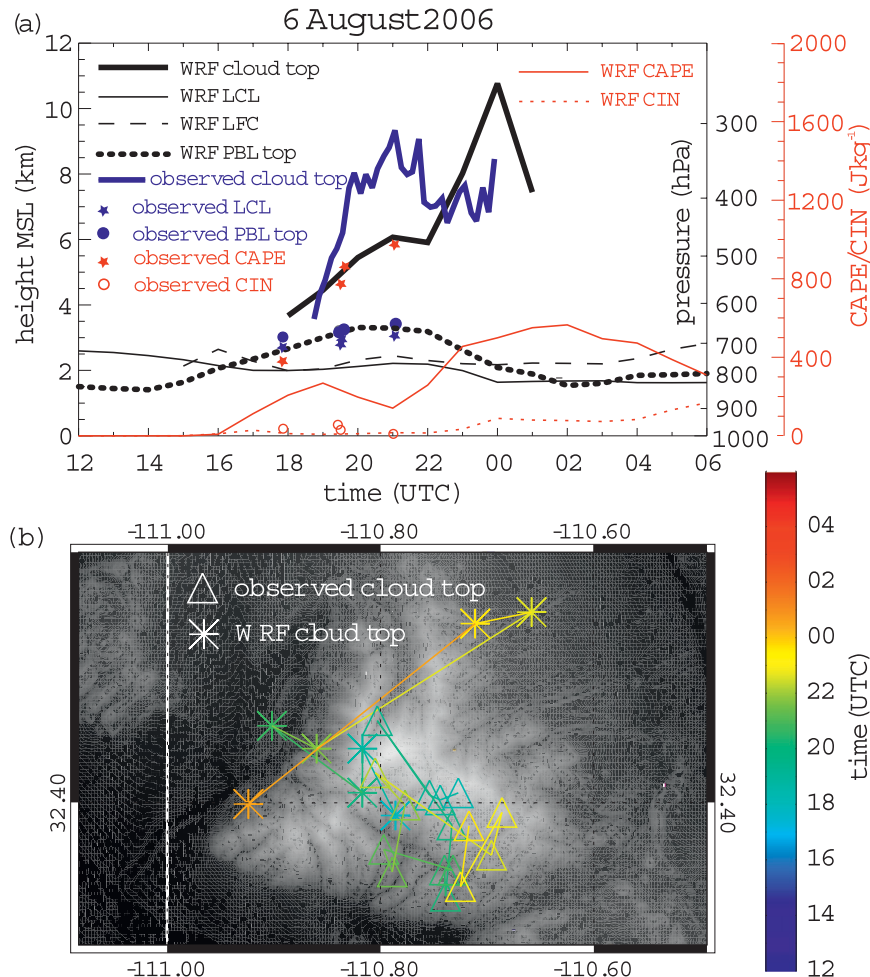


FIG. 4. Trend of observed vs modeled orographic cumulus top evolution. (a) The trend of various stability parameters and of the highest cloud top and (b) the location of the highest cloud top. The time resolution is 20 min for the cloud-top observations and hourly for the model output. The stability parameters are computed from four MGAUS soundings and from model output averaged within the  $30 \times 30 \text{ km}^2$  box shown in Fig. 3. [Note: Lifting condensation level (LCL) and level of free convection (LFC).]

these pressure variations are largely hydrostatic). The convectively induced cold pool produces a dip in anabatic wind forcing at 0000 UTC (higher pressure over the CM). There is a few hours lag between the MSC (Fig. 5c) and the anabatic forcing, which peaks near 2300 UTC according to observations (Fig. 5d) and at 2200 UTC in the model (Fig. 5e). This lag will be revisited later.

### 3. WRF evolution of the boundary layer and orographic convection

#### a. Surface conditions

We now use WRF model output to examine the evolution of the BL flow and its interaction with orographic convection (Figs. 6 and 7). At 1200 UTC, 30 min before

sunrise, drainage flow is simulated in valleys within the CM range, spreading over the adjacent broad valleys to the west and east of the CM. The potential temperature map (Fig. 6a) matches the terrain map (Fig. 3). Anabatic flow is first evident at 1500 UTC, mainly on the east side of the CM, as the deepening CBL ingests some easterly momentum from higher levels (Fig. 2). By 1900 UTC the CM is well within the CBL (Fig. 4a), but the elevated terrain retains a higher surface  $\theta$  than the surrounding lowlands. During much of the day and mainly between 1800 and 2100 UTC, the CBL  $\theta$  is higher, and the CBL deeper, in the San Pedro valley to the east of the CM (Fig. 3), compared to the Tucson valley to the west. This pattern is recurrent in WRF simulations, including the two cases in Part I. Unlike most other days, the ISFF observations do not confirm such east–west difference

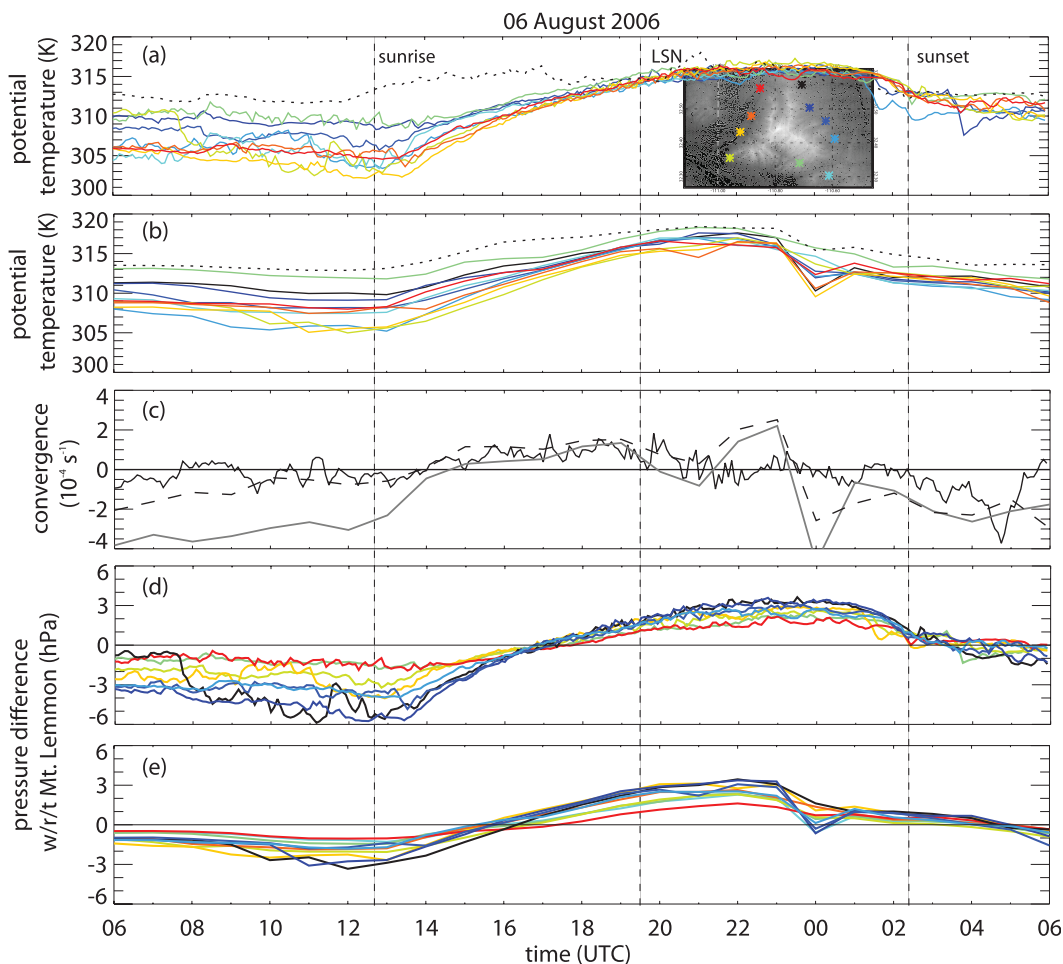


FIG. 5. Comparison of observed vs WRF-simulated surface parameters. (a) Observed potential temperature at Mt. Bigelow (dashed black line) and at the ISFF stations, color coded as shown in the insert terrain map; (b) as in (a), but from WRF model output; (c) observed (solid black line) and modeled (gray line) surface MSC calculated from the 10 ISFF stations and modeled surface MSC into the  $30 \times 30 \text{ km}^2$  box shown in Fig. 3 (dashed line); (d) observed horizontal pressure difference between the ISFF stations and the mountain top [following Geerts et al. (2008), positive values imply a lower pressure over the mountain]; and (e) as in (d), but from WRF model output. The dark blue ISFF station (Stratton Canyon) was also the MGAUS release site on this day. The vertical dashed lines indicate the times of sunrise, local solar noon (LSN), and sunset.

on 6 August (Fig. 5a), probably because much rain had fallen on the east side of the CM during the previous days.

A sinuous meridional convergence line can be seen over the CM starting at 1600 UTC, prior to moist convection (dashed blue line in Fig. 8a). This boundary results from the confluence of anabatic flow from opposite sides of the CM spine, which is roughly north–south oriented (Fig. 3). It is best defined at 1800 UTC (Figs. 6c and 8c), with cumulus developing above. Mainly the southern half of this boundary slowly propagates westward in the early afternoon, not by solenoidal forcing (the higher temperature on the east would result in eastward propagation) but because of the prevailing easterly flow (Figs. 2 and 6). Convective initiation along a convergence

line drifting downwind from the crest has been observed elsewhere (e.g., Banta 1984). Cumulus develops along this boundary through 0000 UTC, mainly over the highest terrain, especially near Pusch Ridge (Fig. 3), where persistent convergent flow leads to increasingly deep convection (Figs. 8c–f). The boundary becomes less defined as a result of convective outflows (Figs. 8d,e).

Surface MSC over the CM increases steadily until 1800 UTC (Fig. 5c). It decreases slightly as rather shallow convection develops and matures between 1900 and 2100 UTC, but over a broader scale (e.g., in a  $40 \times 40 \text{ km}^2$  square around the CM) it continues to increase until the effects of deeper convection peaking at 0000 UTC are felt (not shown). Orographic Cu continues to deepen (Fig. 4a)

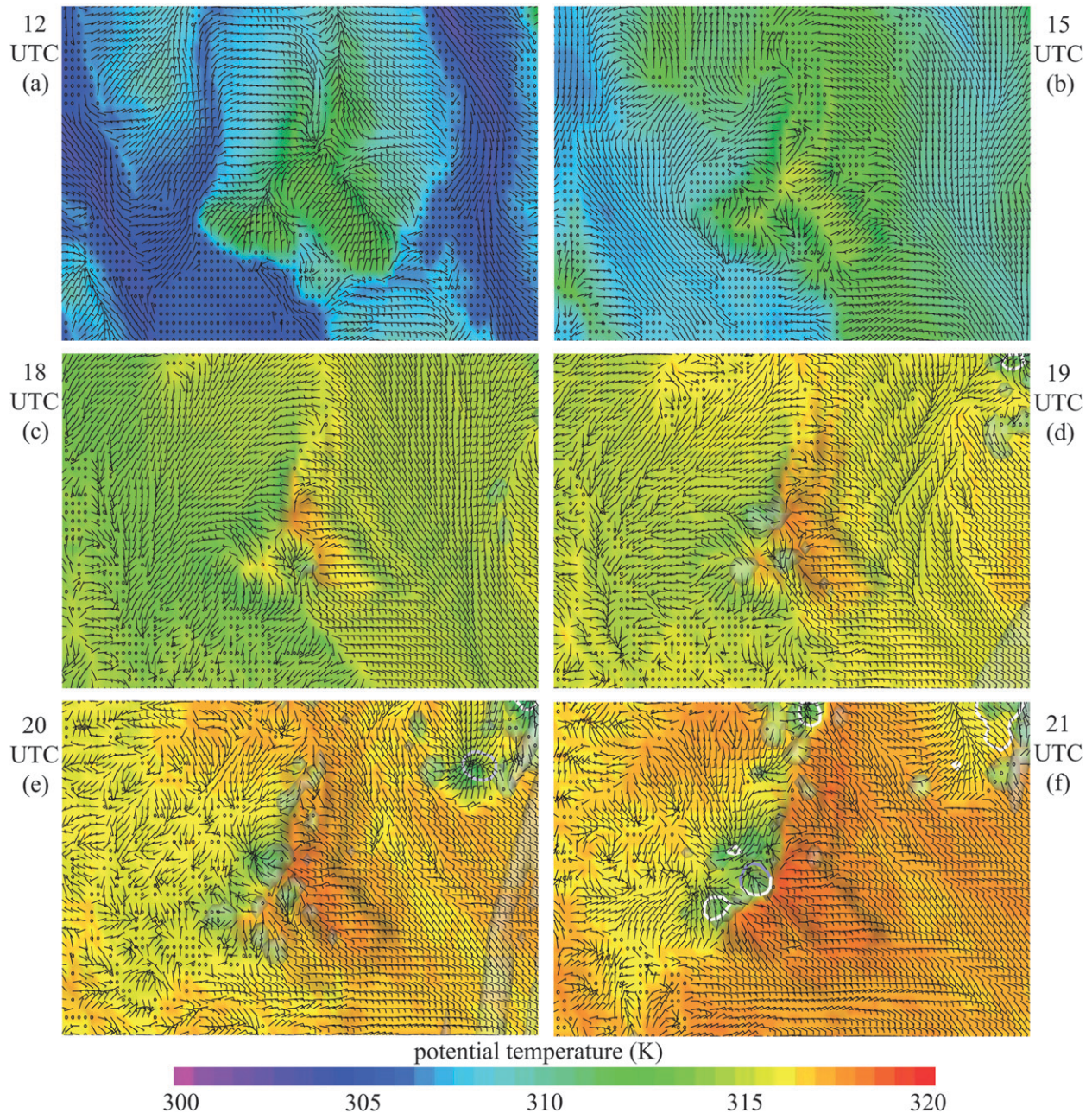


FIG. 6. Inner-domain maps of 2-m  $\theta$  (color) draped over the terrain and 10-m winds (thin barb) for 1200, 1500, 1800–2100 UTC 6 Aug 2006. Also shown are the  $0.01 \text{ g kg}^{-1}$  cloud water isosurfaces (transparent) and 1-h accumulated precipitation with contours of 0.25 (white), 2.5 (blue), 6.4 (light blue), and 12.7 mm (light green).

with a trace of precipitation first falling at 2100 UTC over Pusch Ridge and near Mt. Lemmon (Fig. 6f). The cooling (locally up to 4 K) due to cloud shading, the evaporation of rain, and the downward transport of low  $\theta_e$  results in a decrease in MSC at this time (Fig. 5c). Convection is suppressed during the next hour (Fig. 4a) and no precipitation occurs (Fig. 7a). This evolution is similar to the 9 July 2006 case analyzed in Part I.

But unlike the 9 July case, new Cu develop over the CM at 2200 UTC as the cold pools are advected off the mountain and warm air is reestablished over the highest terrain (Fig. 7a). As a consequence, a sharp increase of MSC occurs between 2100 and 2300 UTC (Fig. 5c). Specifically, a cell of deep convection develops just north of Pusch Ridge (Fig. 7b). Precipitating convection also develops in the San Pedro Valley



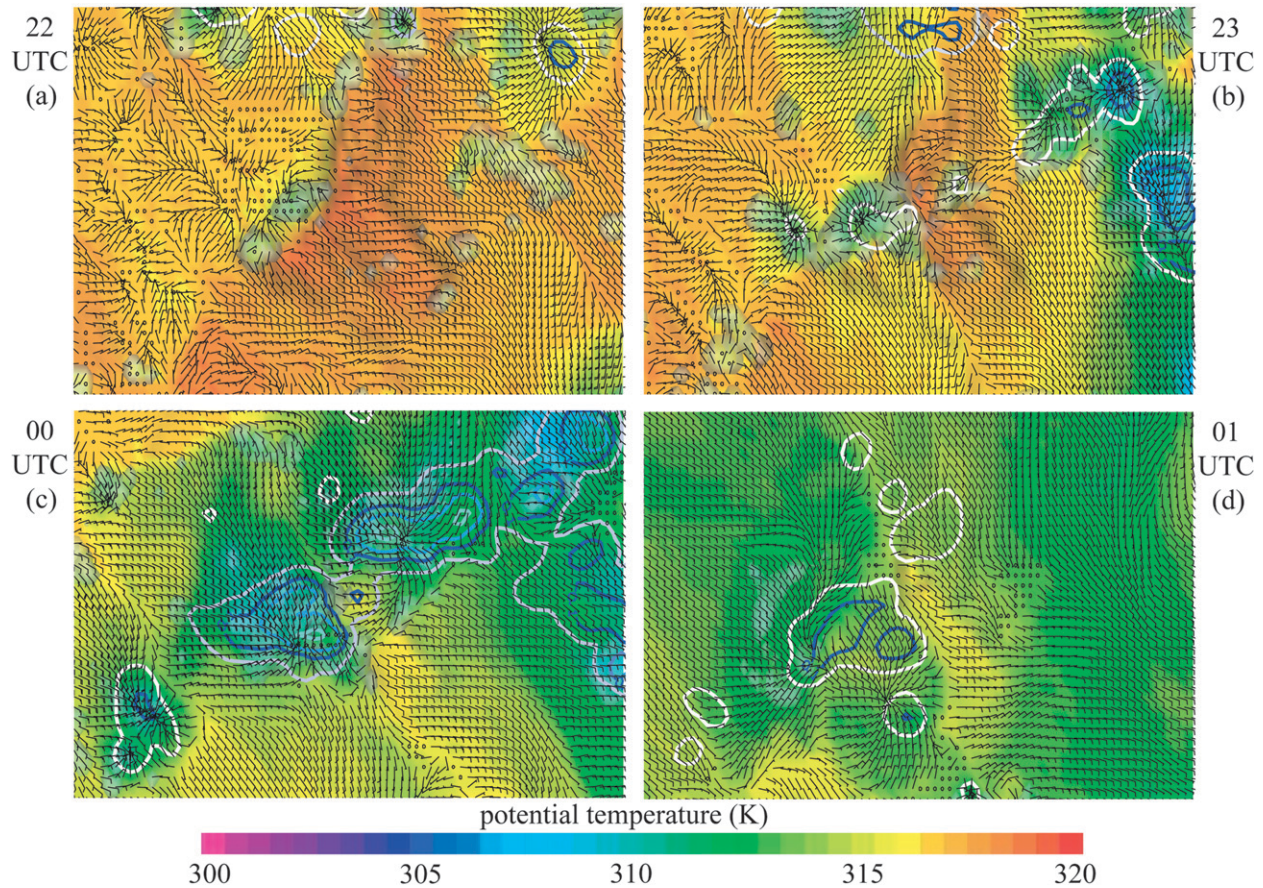


FIG. 7. As in Fig. 6, but for 2200–0100 UTC.

during this period, still well within the model’s inner domain.

Convective evolution over the CM becomes rather complex at 2300–0000 UTC, with secondary convective initiation due to outflow boundaries colliding with the terrain, with another outflow boundary, or with channels of upslope flow. For instance, the outflow from the Pusch Ridge cell produces a secondary cell over Bear Canyon (see Fig. 3), yielding the deepest tower of the day at 0000 UTC. Most precipitation accumulated on this day falls from these two cells, with a maximum of  $14 \text{ mm h}^{-1}$  (Fig. 7c). This complex outbreak of deep convection results in divergent surface flow around the CM, starting at 0000 UTC and continuing into the night (Fig. 5c). Weak anabatic forcing is restored for a few hours (Fig. 5e), but it does not result in net convergent flow at the surface. At 0100 UTC, only anvils remain over the mountain footprint and precipitation ends (Fig. 7d).

*b. Solenoidal circulation and its forcing*

In Part I we argued that some temporal or spatial averaging is needed to isolate the solenoidal forcing and

the resulting circulation in the BL. To retain good temporal resolution in an east–west cross section, we average across 21 km in the north–south direction, which corresponds with the long axis of the CM chain (Fig. 3) and is normal to the prevailing wind (Fig. 2). Because the San Pedro valley to the east becomes warmer than the Tucson valley to the west during the day (Fig. 6), we remove the mean potential temperature on each side of the mountain ( $\overline{\theta}_{\text{east}}$  and  $\overline{\theta}_{\text{west}}$ , respectively) at any pressure level, and plot the residual anomalies ( $\theta'$ ). The vertical profiles of  $\overline{\theta}_{\text{east}}$  and  $\overline{\theta}_{\text{west}}$  are shown in a side panel in Fig. 9. The departure ( $u'$ ) from the mean zonal wind across the entire length of the cross section ( $\overline{u}$ ) is contoured in Fig. 9. The profile of  $\overline{u}$  is shown in the right-hand-side panel in Fig. 9.

The predawn hours (1200 UTC) witness shallow drainage flow with a peak magnitude of  $3 \text{ m s}^{-1}$  on both sides. The easterly stratified flow aloft accelerates slightly just downstream of the mountain and experiences some lee-wave motion. Shallow anabatic flow, approximately  $1 \text{ m s}^{-1}$  in strength, develops by 1500 UTC (Fig. 9b). This is in response to a shallow warm anomaly, initially

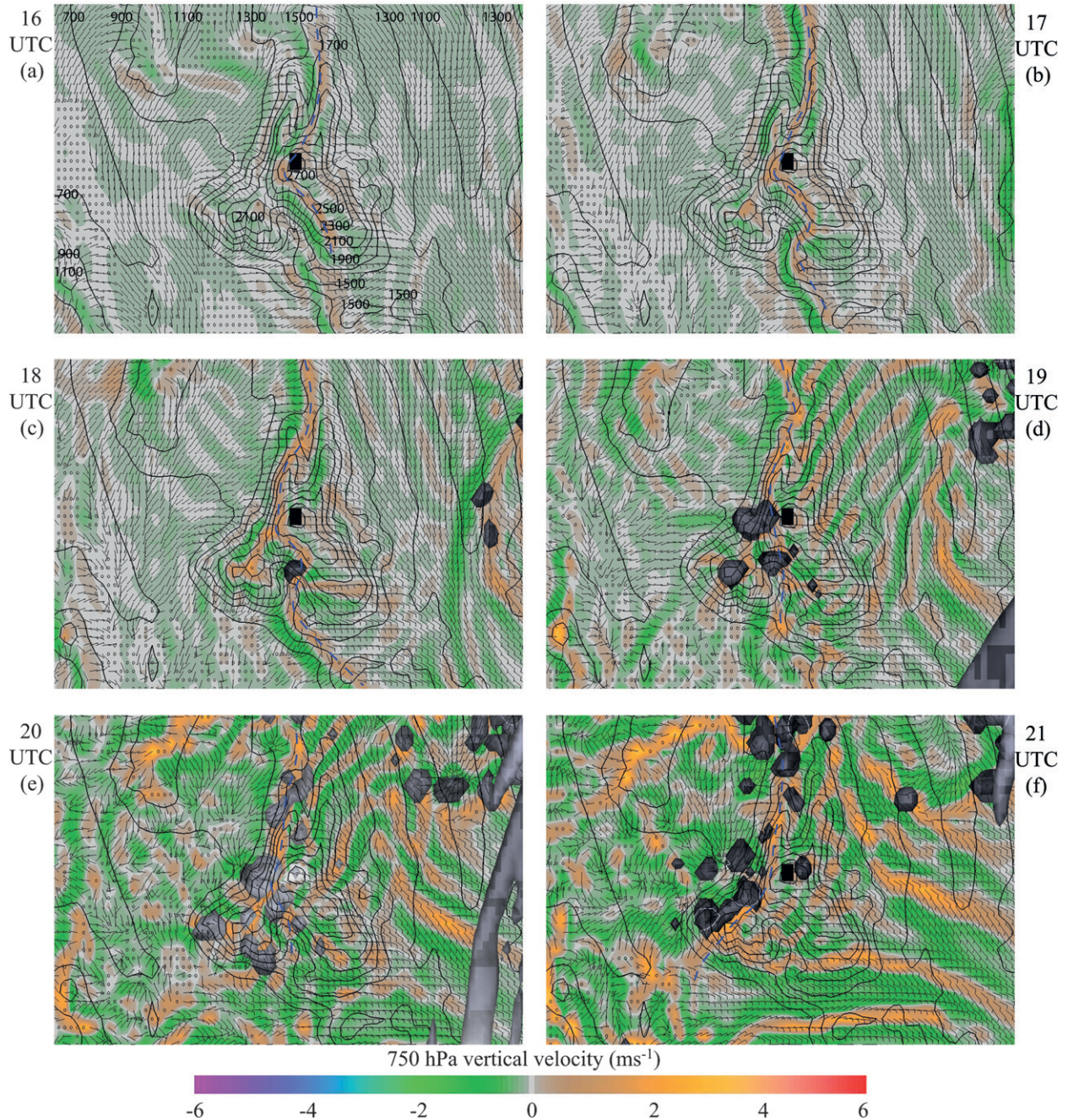


FIG. 8. Inner-domain maps of 750-hPa vertical velocity ( $\text{m s}^{-1}$ ) and 10-m winds (thin barbs) for (a)–(f) 1600–2100 UTC 6 Aug 2006. Also shown are the  $0.01 \text{ g kg}^{-1}$  cloud water isosurfaces and elevation contours (black) with an interval of 200 m [labeled in (a)]. The black rectangle in the vertical velocity field is due to Mt. Lemmon's elevation, slightly above the 750-mb surface. The dashed blue line in (a)–(f) highlights a convergence line discussed in the text.

just on the eastern slopes, but by 1700 UTC more uniformly distributed across the mountain, and over a depth corresponding to that of the anabatic circulation.

By 1800 UTC (Fig. 9c), the time that the first orographic Cu appear in the WRF simulation, the PBL has deepened, especially over the San Pedro valley and over

the CM, and vertical velocities in the CBL have increased. An updraft peaking at  $0.8 \text{ m s}^{-1}$  is found just west of the mountain. This updraft is coincident with the convergence line mentioned before (Fig. 8c). The anabatic circulation has strengthened to  $2 \text{ m s}^{-1}$  on both sides and has deepened to encompass the lower half of the

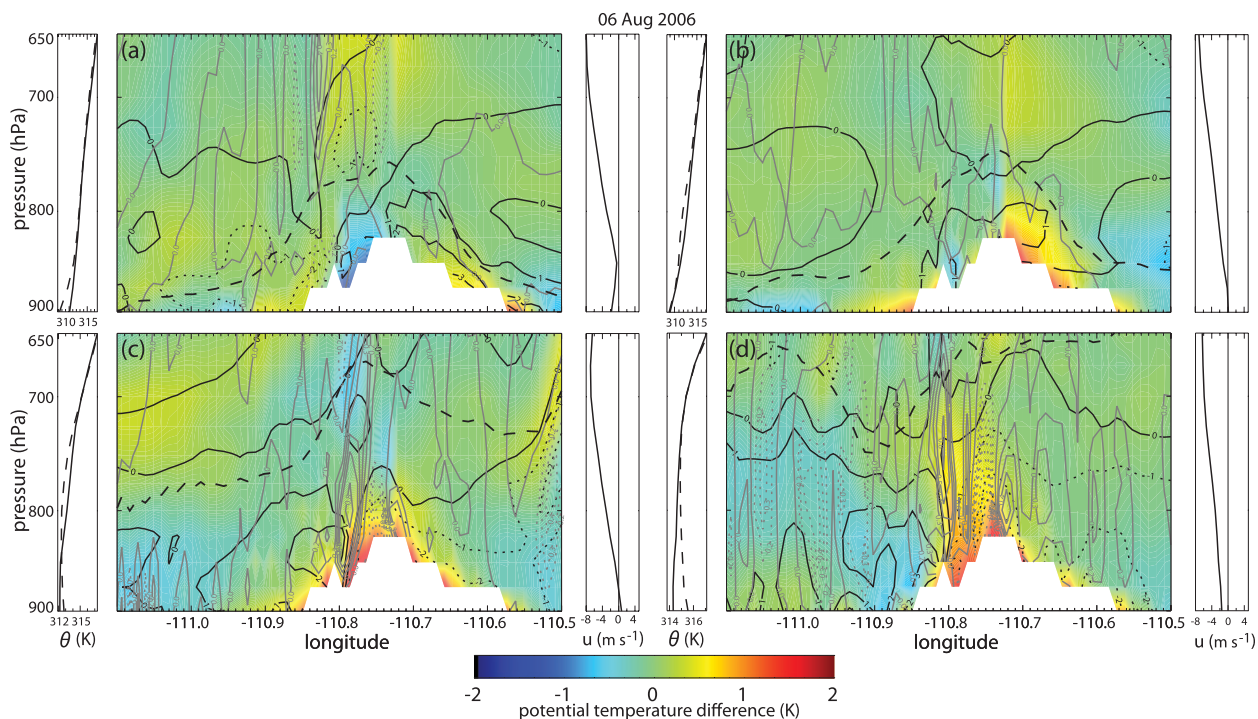


FIG. 9. East–west cross section based on averages computed over 21 km in the north–south direction for (a) 1200, (b) 1500, (c) 1800, and (d) 2100 UTC. The white area is the 21-km-averaged terrain height. The cross section shows  $\theta'$  (color fill),  $u'$  (solid black contours for westerly flow and dotted black contours for easterly flow, contour interval  $1 \text{ m s}^{-1}$ ),  $w$  (solid gray contours for updrafts and dotted gray contours for downdrafts, contour interval  $0.2 \text{ m s}^{-1}$ ), and PBL height (long-dashed black line). Also shown are profiles of  $\overline{\theta}_{\text{west}}$  (solid) and  $\overline{\theta}_{\text{east}}$  (dashed) on the left of each cross section, and  $\overline{u}$  on the right. The variables are defined in the text.

CBL. In the upper CBL weak divergent flow ( $\sim 1 \text{ m s}^{-1}$ ) and a cold anomaly have developed, consistent with the two cases in Part I.

At 2100 UTC, three updraft regions exist (Fig. 9d). The westernmost one is the deepest and strongest ( $0.8 \text{ m s}^{-1}$ ) and roughly corresponds with the convergence line in Fig. 8f. It is coincident with the deep convergence of anabatic flow ( $\sim 2 \text{ m s}^{-1}$  in strength) from the west and the east, the latter spilling over the high ridge due to prevailing easterly flow. The warm anomaly is  $\sim 1 \text{ km}$  deep (cf. the depth of the anabatic flow),  $\sim 15 \text{ km}$  wide, and  $1\text{--}1.5 \text{ K}$  strong, which makes this case similar to the Cu congestus case (9 July) presented in Part I. Very weak return (divergent) flow exists above the warm anomaly and is still largely contained within the CBL. The strength and depth of the low-level anabatic flow (cf. the return flow) suggests that at this time BL air is transported into the free atmosphere above the PBL. This will be examined in more detail later. Cross sections for later times (2300–0000 UTC) are not shown in Fig. 9, because by then deep convection has developed, with convectively induced cold pools and convergence zones, and updrafts whose maxima are above the top of the display in Fig. 9.

*c. Mountain-scale convergence and its forcing*

To examine the vertical profile of convergence at the scale of the mountain, we use the  $30 \times 30 \text{ km}^2$  box centered on Mt. Lemmon shown in Fig. 3. This box encompasses the majority of the CM and generally does not intersect high terrain. Other boxes with the same center have been examined as well, from  $10 \times 10 \text{ km}^2$  to  $40 \times 40 \text{ km}^2$ , but we only show the 30-km dimension because the results from other boxes are not fundamentally different, and because 30 km is a representative diameter of the CM. Also, the  $30 \times 30 \text{ km}^2$  encapsulates the drifting convergence line (mentioned in section 3a) during its lifetime, whereas the smaller boxes do not. Note that the surface MSC (based on 10-m winds) is not computed at a constant pressure level, but rather along the undulating terrain of the box perimeter. In Fig. 10, the surface MSC is assigned an altitude corresponding with the average surface pressure along this perimeter. Constant-pressure MSC values are only available above the highest terrain elevation along the box perimeter (i.e., at 840 hPa), a level considerably above the mean altitude of the surface MSC (895 hPa). Thus, Fig. 10 contains no information between 895 and

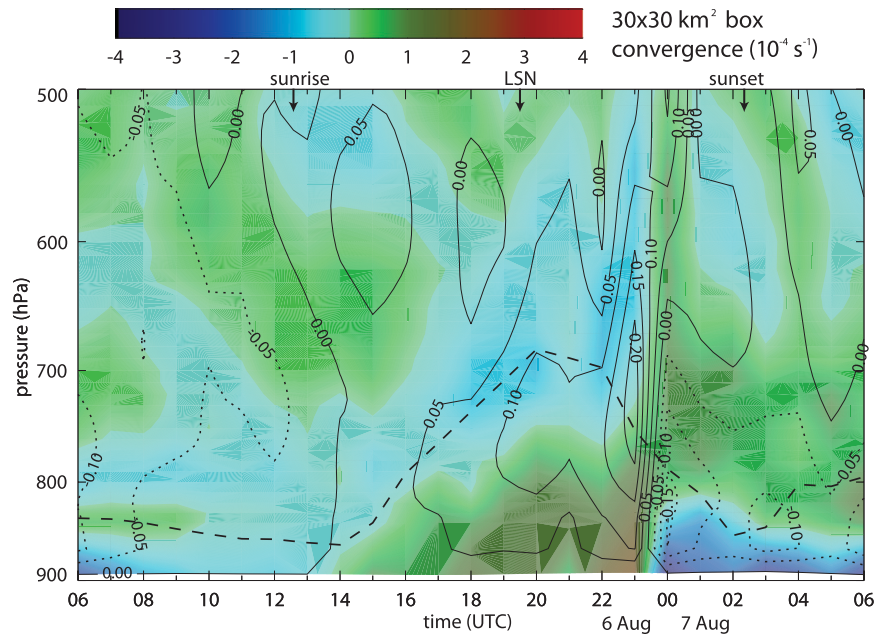


FIG. 10. Time–height plot of MSC for the  $30 \times 30 \text{ km}^2$  box (color shaded), mountain-scale vertical velocity within this box, inferred from mass continuity (solid lines for updrafts, dotted lines for downdrafts, and contour interval  $0.05 \text{ m s}^{-1}$ ), and mean PBL height within the box (bold dashed line).

840 hPa. Starting at 840 hPa, the vertical resolution is 20 hPa.

The surface flow becomes convergent at 1400 UTC,  $\sim 1.5$  h after sunrise (Fig. 10). The convergent layer deepens at the same rate as the CBL through 1700 UTC. Weak divergence near the CBL top develops after 1800 UTC, with a level of nondivergence in the upper CBL throughout the afternoon until deep convection erupts. The surface flow becomes weakly divergent at 2100 UTC due to cloud shading and cold-pool dynamics associated with Cu congesti. These clouds transport BL air up above the PBL top, with divergence out of the  $30 \times 30 \text{ km}^2$  box into the lower free troposphere, up to 520 hPa. Lower-CBL MSC intensifies again between 2100 and 2300 UTC, generating a maximum mountain-scale vertical velocity of  $0.2 \text{ m s}^{-1}$  near the PBL top. This updraft transports CBL air into the free atmosphere over greater depths, up to  $\sim 300$  hPa. The maturing of deep convection at 0000 UTC leads to strong near-surface divergence, resulting in a dipole of extreme values that stands out in the 12-h-long time–height transect of Fig. 10. Near-surface divergence continues into the evening, as convection decays and shallow katabatic flow develops. Convergent flow persists in the residual CBL above the surface stable layer until 0600 UTC because the horizontal pressure gradient remains anabatic through 0600 UTC, for all points on the perimeter of the  $30 \times 30 \text{ km}^2$  box (Fig. 11a). In the 6 August case

the surface flow becomes divergent 1.5 h earlier in the afternoon than on the dry day in Part I, on account of the convective outflows. If the deep convection had occurred earlier, anabatic flow likely would have been restored, given the strong anabatic forcing (Fig. 11a).

In the evening the surface flow becomes disconnected from the pressure gradient force, which operates over a greater depth. The horizontal pressure gradient force at the  $30 \times 30 \text{ km}^2$  scale (derived as in Part I) appears largely immune to the convective development simulated for 6 August (Fig. 11a). The effect of deep convection on horizontal pressure variations is more evident at the smaller scale of the convective cold pool; for instance, a weak high temporarily forms over Mt. Lemmon relative to points along a  $10 \times 10 \text{ km}^2$  square at 0000 UTC (Fig. 11b). It is also more evident in the ISFF station record for this day (Fig. 5d). Deeper or larger convection is likely to produce a stronger high during its decay phase, thus affecting the pressure gradient pattern more, as observed (Geerts et al. 2008). At smaller scales the extreme pressure differences are smaller, but the MSC values are generally higher (Fig. 11).

Evening convergence in the residual CBL above a shallow stable layer occurs on all CuPIDO days simulated, including the two cases in Part I. It is stronger than the convergence needed to compensate for the surface katabatic flow. It remains an open question whether or not this elevated MSC can trigger moist convection, and

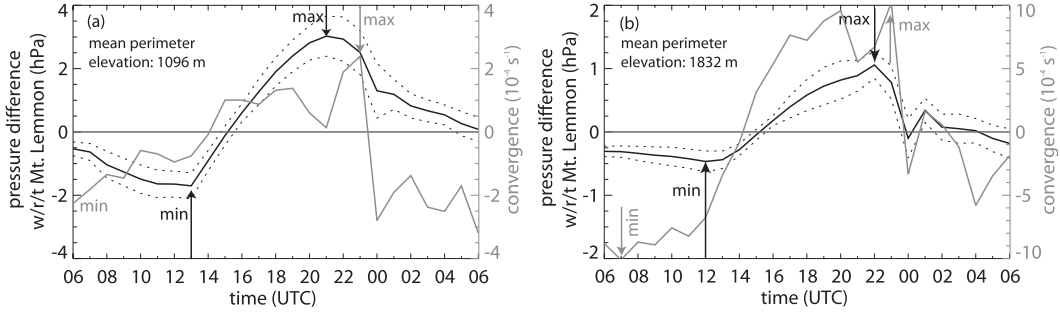


FIG. 11. (a) Time series of the mean horizontal pressure difference between points along the  $30 \times 30 \text{ km}^2$  box and Mt. Lemmon (black solid line, left axis), and MSC for the corresponding box (gray lines, right axis), for the 6 Aug 2006 case. The black dotted lines indicate the mean pressure difference  $\pm 1$  standard deviation, based on all grid points of the box's perimeter. A positive pressure difference implies a lower pressure at Mt. Lemmon (i.e., anabatic "forcing"). Black arrows highlight the times of extreme pressure differences. Gray arrows highlight the same for MSC. The average height of points along the box perimeter is shown in the top-left corner. For comparison, the elevation of Mt. Lemmon in the inner WRF domain is 2629 m MSL. (b) As in (a), but for a  $10 \times 10 \text{ km}^2$  box centered on Mt. Lemmon.

whether such vespertal convective initiation is affected by afternoon convection. On 6 August 2006, no additional convection developed after the afternoon convection ceased at 0100 UTC, but vespertal convective initiation over the CM occurred on several other days in CuPIDO.

#### 4. Mass, moisture, and heat budget

##### a. Mass flux

We now examine fluxes in and out of three volumes with fixed horizontal dimensions (i.e., the  $30 \times 30 \text{ km}^2$  box) and with variable vertical boundaries: surface to  $0.5z_i$  for volume 1,  $0.5z_i$  to  $z_i$  for volume 2, and  $z_i$  to the highest cloud top within the box (Fig. 4) for volume 3. Here  $z_i$  is the average PBL top within the box. WRF uses a terrain-following vertical coordinate (sigma). Thus, the vertical boundaries of the volumes, expressed in terms of sigma levels, do not intersect the terrain (Fig. 12d). Using the notation in Skamarock et al. (2008), the air-mass continuity equation is

$$\frac{\partial \mu}{\partial t} = -\nabla_h \cdot (\mu \mathbf{v}_h) - \frac{\partial \mu \dot{\eta}}{\partial \eta}, \quad (1)$$

where  $\mu = p_{\text{hs}} - p_{\text{ht}}$  is the difference in hydrostatic pressure at the surface ( $p_{\text{hs}}$ ) and the top of the model domain ( $p_{\text{ht}}$ ),  $\eta = (p_h - p_{\text{ht}})/\mu$  is the mass vertical coordinate,  $p_h$  is the hydrostatic component of the total air pressure,  $\eta = D\eta/Dt$  is the total derivative of  $\eta$  and thus the "vertical" velocity in this coordinate system, and  $\mathbf{v}_h$  is the horizontal velocity vector. We integrate (1) across a volume with area  $A$  and vertical bounds  $\eta_1$  and  $\eta_2$ :

$$\int_{\eta_1}^{\eta_2} \int_A \frac{\partial \mu}{\partial t} dA d\eta = - \int_{\eta_1}^{\eta_2} \int_A \nabla_h \cdot (\mu \mathbf{v}_h) dA d\eta - \int_A \int_{\eta_1}^{\eta_2} \frac{\partial \mu \dot{\eta}}{\partial \eta} d\eta dA. \quad (2)$$

The use of the divergence theorem and division by the volume  $A\Delta\eta$  yields

$$\frac{\partial \bar{\mu}}{\partial t} = \frac{1}{A\Delta\eta} \int_{\eta_1}^{\eta_2} \left( \oint_S \mu v_n ds \right) d\eta + \frac{1}{A\Delta\eta} \int_A (\mu \dot{\eta})_1 - (\mu \dot{\eta})_2 dA, \quad (3)$$

where  $v_n$  is the wind component normal to the perimeter  $s$  of area  $A$ , is positive inward, and the overbar indicates a volume average. The term on the left in (3) is the change in mass within the volume, which is a function of the mean temperature. The first integral term on the right in (3) is the net horizontal mass flux across the lateral boundaries of the volume, and the second integral is the difference between the net vertical mass flux across the lower and upper boundaries. The integrals are computed as summations with  $\Delta x = \Delta y = 1 \text{ km}$  (120 points along the perimeter of the  $30 \times 30 \text{ km}^2$  box) and over a variable number of vertical levels, with linear interpolation at the edges. The flux terms in (3) are then converted to mass fluxes ( $\text{kg s}^{-1}$ ).

The evolution of the horizontal and vertical mass fluxes for the three volumes is shown in Fig. 12 for the 6 August case. To assess the impact of deep convection on these mass fluxes, the same data are shown in Fig. 12 for a case without any orographic Cu convection (i.e., 12 July 2006), a typical premonsoon day with a deep, weakly capped PBL bulging over the mountain (see Part I for details). For this case, and also for the 6 August case before Cu convection occurs in the  $30 \times 30 \text{ km}^2$  box, the top of the upper volume in (3) is defined arbitrarily as 750 hPa until 1400 UTC (when CBL growth and anabatic flow start) and 400 hPa after 1400 UTC.

More mass converges into the lower PBL ( $\text{HMF}_1$ ; see Fig. 12d for flux labels) and thus more mass is transported into the upper PBL ( $\text{VMF}_1$ ) on the undisturbed day (12 July) than on 6 August, especially in the early

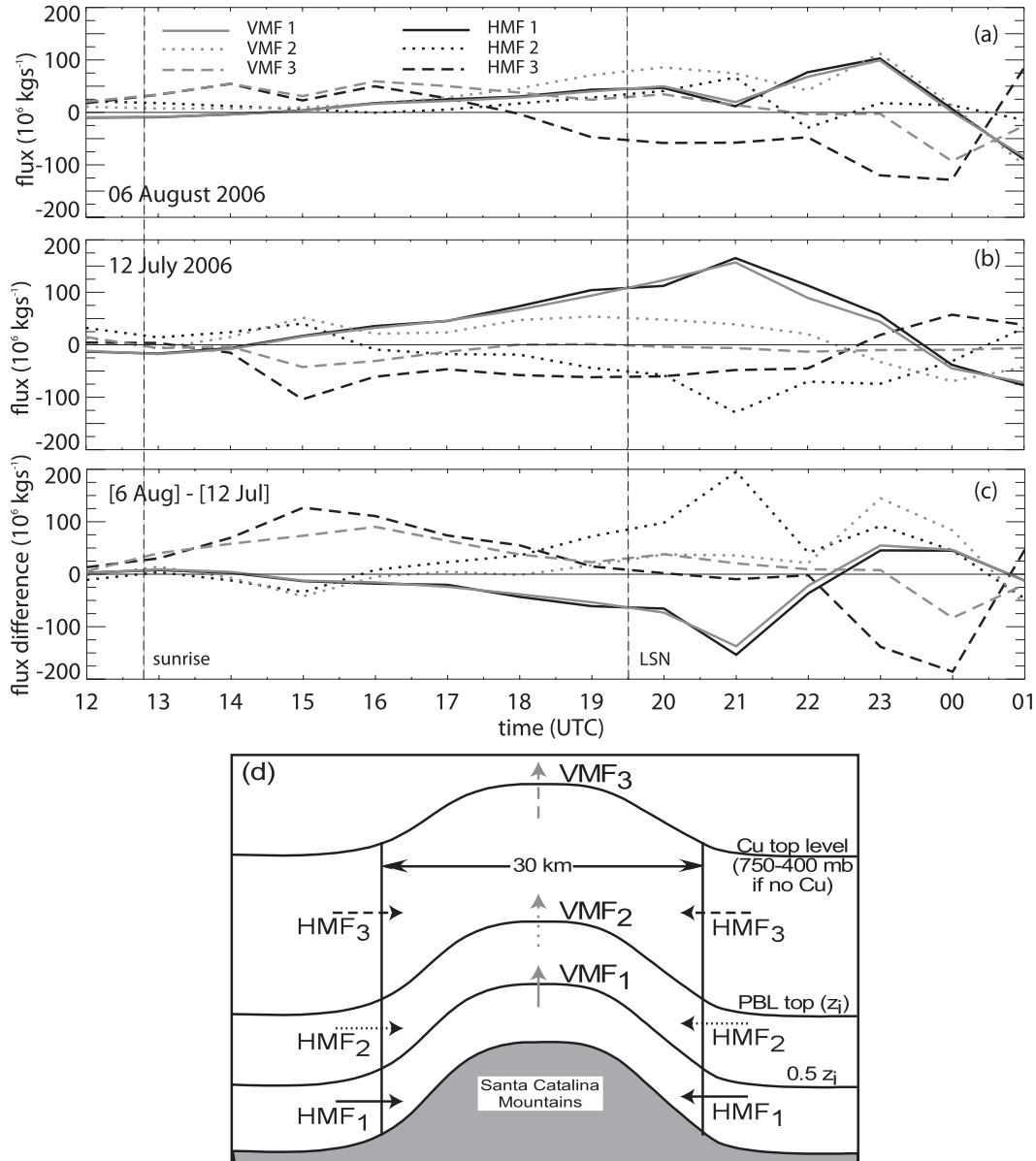


FIG. 12. Temporal variation of the horizontal and vertical mass fluxes in/out three  $30 \times 30 \text{ km}^2$  volumes, for (a) 6 Aug 2006 (a moist case), (b) 12 Jul 2006 (a dry case), and (c) the difference between the moist case and the dry case. (d) Illustration of the three volumes, which are defined in the text. Inward and upward fluxes, shown by the arrows in (d), are positive.

afternoon (Fig. 12). Thus, the orographic solenoidal circulation is stronger on the undisturbed day, and this is due not to a stronger anabatic flow but rather to a deeper CBL; its peak depth is 1.2 km greater on 12 July. When surface heating makes the air over the elevated terrain anomalously warm (Fig. 9), then the solenoidal circulation within the BL advects cooler air. This tends to lower  $\theta_e$  and CAPE, or at least prevents CAPE over the mountain to increase much beyond its value in the surrounding plains. Thus, the suppressed HMF<sub>1</sub> at 2100–2200 UTC

6 August may have been a factor in the rapid increase in CAPE and subsequent convective growth between 2100 and 0000 UTC (Fig. 4a).

On 12 July most of the upward transport VMF<sub>1</sub> diverges from the mountain in the upper PBL (HMF<sub>2</sub> < 0); that is, much of the solenoidal circulation is contained in the PBL (Fig. 12). On 6 August the upper PBL is *convergent* over the mountain (HMF<sub>2</sub> > 0) and significant upward transport into the free troposphere (VMF<sub>2</sub>) occurs. The latter statement is not precise: the *local* PBL top

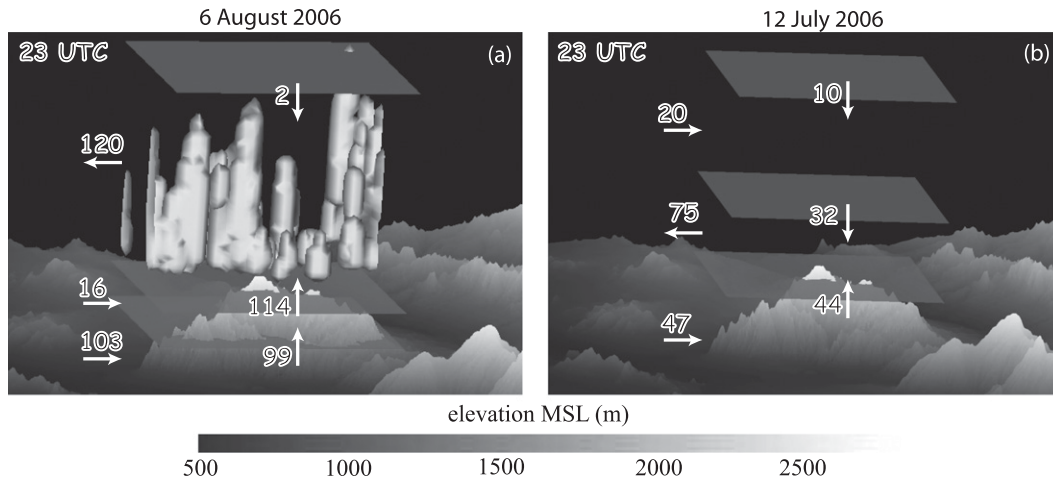


FIG. 13. Horizontal and vertical mass fluxes in/out of the three volumes shown in Fig. 12d at 2300 UTC (a) 6 Aug and (b) 12 Jul 2006. Arrows indicate the direction of flux. Flux quantities are in units of  $10^6 \text{ kg s}^{-1}$ . The terrain and  $0.01 \text{ g kg}^{-1}$  cloud isosurfaces are shown as well. The vertical boundaries of the three volumes are shown schematically as flat surfaces; in reality these boundaries are sigma surfaces undulating with the terrain.

does not exactly coincide with the average PBL top ( $z_i$ ) [although it undulates in a similar fashion over terrain as do sigma surfaces (e.g., Fig. 9)], and thus  $\text{VMF}_2$  is not exactly the flux between the PBL and the free troposphere. As the PBL top bulges more over the mountain than the sigma surfaces on 12 July,  $\text{VMF}_2$  is positive on this day as well, at least until the early afternoon. On 6 August,  $\text{VMF}_2$  grows as convection deepens between 1800–2000 and 2200–2300 UTC (Fig. 4). As convection matures between 2300 and 0000 UTC, strong outflow occurs aloft due to anvil formation ( $\text{HMF}_3 < 0$ ); as it decays between 0000 and 0100 UTC,  $\text{VMF}_2$  becomes negative.

A comparison of the deep convection case with the undisturbed case (Fig. 12c) yields the intuitive result that moist convection suppresses the solenoidal PBL circulation (marked by the combination of  $\text{HMF}_1 > 0$  and  $\text{HMF}_2 < 0$ ) and enhances the transfer of BL air into the free troposphere ( $\text{VMF}_2 > 0$ ) and away from the mountain ( $\text{HMF}_3 < 0$ ). This is illustrated further in Fig. 13 for 2300 UTC, the time of Cb outbreak on 6 August.<sup>2</sup> The PBL was deeper on 12 July, but the mass fluxes are

generally smaller at this time. Orographic convection is fed by inflow not only from the lower PBL but also from the upper PBL, and it disperses the BL air aloft. Thus, the effect of deep orographic convection is to expand the vertical scale of the solenoidal circulation over the mountain from the boundary layer to the troposphere.

The changes in mass flux between the BL and the free troposphere can be attributed more directly to deep convection in a comparison between the default WRF run and a run in which all cloud processes are turned off for the 6 August case. In the no-microphysics run the cloud microphysical, dynamical, and radiative effects of moist convection are disabled. The differences between these simulations (Table 1) obviously are small before convective initiation; for example, the solenoidal circulation within the CBL is only marginally enhanced in the no-microphysics run between 1600 and 2000 UTC (slightly higher  $z_i$ ,  $\text{HMF}_1$ , and  $|\text{HMF}_2|$ ). The deep convection between 2200 and 0000 UTC results in a dramatic increase in mass transport into the CBL over the mountain ( $\text{HMF}_1$  and  $\text{HMF}_2$ ) and more transport up into the free troposphere aloft ( $\text{VMF}_2$ ) and away from the mountain ( $-\text{HMF}_3$ ). Fluxes are reversed during convective decay at 0100 UTC, not just in the PBL but also in the free troposphere. The impact of convection on mass fluxes according to the original versus no-microphysics runs (Table 1) is generally the same in sign and similar in magnitude to the differences between the 6 August and 12 July cases during the period of deep convection (Fig. 12c).

*b. Moisture and heat flux*

We now compare heat and water vapor fluxes over the CM for the deep convection case (6 August) against

<sup>2</sup> It is obvious from Fig. 13 that mass is not precisely conserved in the three volumes. This is partly due to temporal changes in mean density (temperature) within the volume (3) but is mainly because the flow across the volume boundaries is not precisely captured. This is because velocities are staggered one-half grid length from the thermodynamic variables (Skamarock et al. 2008). This offset is especially important in the vertical because the WRF simulation uses only 42 sigma levels and the PBL is a small portion of the model depth. The mass imbalance in any volume is generally less than 10% of the mass fluxes across the volume's boundaries. The differences between the 12 Jul and 6 Aug 2006 cases are far larger, so the comparisons are meaningful.

TABLE 1. The difference in horizontal and vertical mass fluxes for the three volumes illustrated in Fig. 12d between the original and the no-microphysics WRF simulations for 6 Aug 2006. The entire period is broken up in five periods of cumulus evolution. Since  $\text{HMF}_1 \cong \text{VMF}_1$ , the average of these two terms is shown as  $\text{H(V)MF}_1$ .

Time (UTC)		$\text{H(V)MF}_1$ ( $\times 10^6 \text{ kg s}^{-1}$ )	$\text{HMF}_2$ ( $\times 10^6 \text{ kg s}^{-1}$ )	$\text{HMF}_3$ ( $\times 10^6 \text{ kg s}^{-1}$ )	$\text{VMF}_2$ ( $\times 10^6 \text{ kg s}^{-1}$ )	$\text{VMF}_3$ ( $\times 10^6 \text{ kg s}^{-1}$ )
1200	Cloud free	0	0	-10	0	-9
1300		0	-1	-9	-1	-9
1400		0	-3	+9	-3	+5
1500		0	-1	+1	-2	-2
1600	Preconvective	+8	+5	-9	+12	+3
1700		+9	-4	-10	+6	-3
1800	Shallow convection	+5	-7	-6	0	-6
1900		-4	-1	-2	-1	-1
2000		+13	-17	+14	-2	+9
2100		-34	+33	+9	-2	+5
2200	Deep convection	+75	-59	-26	+14	-4
2300		+129	+33	-154	+154	+10
0000		+13	+24	-57	+37	-11
0100	Decay	-133	-76	+196	-194	-27

those for the dry case (12 July). These fluxes are defined as follows for a volume with vertical bounds ( $\eta_1, \eta_2$ ) and horizontal area  $A$ :

$$\begin{aligned} \text{horizontal heat flux (HHF)} &: \frac{C_p}{A\Delta\eta} \int_{\eta_1}^{\eta_2} \left( \oint_s \theta \mu v_n ds \right) d\eta, \\ \text{horizontal vapor flux (HVF)} &: \frac{1}{A\Delta\eta} \int_{\eta_1}^{\eta_2} \left( \oint_s q_v \mu v_n ds \right) d\eta, \\ \text{vertical heat flux (VHF)} &: \frac{C_p}{A\Delta\eta} \int_A \theta \mu \dot{\eta} dA, \quad \text{and} \\ \text{vertical vapor flux (VVF)} &: \frac{1}{A\Delta\eta} \int_A q_v \mu \dot{\eta} dA, \end{aligned} \quad (4)$$

where  $C_p$  is the specific heat under constant pressure and  $q_v$  is the specific humidity. The flux terms in (4) are converted to units of watts and kilograms per second for heat and vapor fluxes, respectively. Neither heat nor water vapor is generally conserved in any volume and subgrid-scale eddy fluxes are nonzero, so the net fluxes across the boundaries of a volume are not generally zero even if the mass fluxes balance. Table 2 summarizes the differences in the horizontal and vertical transport of sensible heat and vapor between the thunderstorm case and the dry case for the two PBL volumes.

Because of a deeper solenoidal circulation (Fig. 12), more sensible heat converges into the lower CBL over the mountain ( $\text{HHF}_1$ ), is carried up ( $\text{VHF}_1$ ), and diverges in the upper CBL ( $\text{HHF}_2$ ) on the dry day (12 July), during 7 h centered at solar noon. The same applies to water vapor, even though the average mixing ratio was lower on the dry day. The moist convection over the CM on 6 August (1800–0000 UTC) transports more vapor ( $\text{VVF}_2$ )

and sensible heat ( $\text{VHF}_2$ ) into the free troposphere than on 12 July, and some of this vapor and heat is drawn in from the upper CBL ( $\text{HVF}_2 > 0$  and  $\text{HHF}_2 > 0$ ). The outbreak of deep convection on 6 August is responsible for 38 tW of extra heat and nearly 1 kiloton of extra water vapor ( $98 \times 10^4 \text{ kg s}^{-1}$ ) drawn into the CBL over the mountain (in comparison to the 12 July case; 2300–0000 UTC data averaged). Most of that extra heat (37 tW) and water vapor ( $95 \times 10^4 \text{ kg s}^{-1}$ ) is pumped into the free troposphere, where it feeds the convection (Table 2). As convection decays at 0100 UTC 6 August, and convective downdrafts and outflows dominate, the flux differences change sign, and some heat and moisture are returned to the PBL.

TABLE 2. The difference in horizontal and vertical heat and vapor fluxes for volumes 1 and 2 (illustrated in Fig. 12d) between 6 Aug and 12 Jul 2006 based on WRF model output. The boldface numbers represent hours with moist convection over the CM on 6 Aug 2006. Local solar noon is at 1929 UTC.

Time (UTC)	$\text{HHF}_1$ (tW)	$\text{HHF}_2$ (tW)	$\text{HVF}_2$ ( $\times 10^4 \text{ kg s}^{-1}$ )	$\text{VHF}_1$ (tW)	$\text{VHF}_2$ (tW)	$\text{VVF}_2$ ( $\times 10^4 \text{ kg s}^{-1}$ )
1200	+1	-3	-10	+1	-1	-6
1300	+3	+1	+5	+3	+4	+7
1400	+1	-4	-6	+1	-2	-8
1500	-4	-11	-23	-4	-13	-30
1600	-6	+3	+18	-5	-2	-6
1700	-7	+7	+42	-8	+1	+11
<b>1800</b>	<b>-14</b>	<b>+12</b>	<b>+46</b>	<b>-13</b>	<b>-1</b>	<b>+18</b>
<b>1900</b>	<b>-20</b>	<b>+23</b>	<b>+73</b>	<b>-18</b>	<b>+5</b>	<b>+34</b>
<b>2000</b>	<b>-22</b>	<b>+32</b>	<b>+80</b>	<b>-25</b>	<b>+12</b>	<b>+38</b>
<b>2100</b>	<b>-51</b>	<b>+64</b>	<b>+141</b>	<b>-46</b>	<b>+11</b>	<b>+52</b>
<b>2200</b>	<b>-12</b>	<b>+14</b>	<b>+21</b>	<b>-8</b>	<b>+6</b>	<b>+31</b>
<b>2300</b>	<b>+15</b>	<b>+31</b>	<b>+91</b>	<b>+16</b>	<b>+46</b>	<b>+136</b>
<b>0000</b>	<b>+16</b>	<b>+14</b>	<b>+36</b>	<b>+15</b>	<b>+28</b>	<b>+53</b>
<b>0100</b>	<b>-2</b>	<b>-12</b>	<b>-23</b>	<b>-4</b>	<b>-17</b>	<b>-101</b>



The water vapor flux calculations allow an estimation of the average precipitation efficiency over the CM for the 6 August case. Precipitation efficiency (PE) is the fraction of all condensed water in a storm that precipitates on the earth surface (e.g., Braham 1952; Auer and Marwitz 1968; Hobbs et al. 1980; Jiang and Smith 2003; Fuhrer and Schär 2005). Practically, we define the PE as the ratio of the  $30 \times 30 \text{ km}^2$  integrated surface precipitation rate ( $P_{\text{sfc}}$ ) to  $\text{VVF}_2$ , since the cloud base [lifting condensation level (LCL)] is close to the average PBL top (Fig. 4a). To place PE in context, we ask what happens to the water vapor drawn into the base of cumulus clouds over the mountain ( $\text{VVF}_2$ ). As a first approximation, for a steady-state storm that remains within the  $30 \times 30 \text{ km}^2$  box over the mountain:

$$\text{VVF}_2 \approx P_{\text{sfc}} + E_{\text{PBL}} - \text{HVF}_3 + \text{VVF}_3 - \text{HIF}_3 + \int_{V_3} \rho \Delta q_v dV \text{ (kg s}^{-1}\text{)}, \quad (5)$$

where the subscripts refer to the volumes as in Fig. 12d,  $E_{\text{PBL}}$  is the evaporation of rain below cloud base (specifically, within volumes 1 and 2), and  $\text{HIF}_3$  represents the horizontal ice flux owing to anvils spreading outside the  $30 \times 30 \text{ km}^2$  box;  $P_{\text{sfc}}$  is estimated as the average precipitation rate during the past hour. The last term in (5) is the change in storage of water vapor in the upper volume 3 ( $V_3$ ) by detraining convection, also evaluated over the past hour. A significant fraction of this volume becomes cloudy as deep convection breaks out on 6 August (Fig. 13). Yet this term is insignificant compared to  $P_{\text{sfc}}$  when the convection is intense. The terms  $\text{VVF}_3$  and  $\text{HIF}_3$  also prove to be negligibly small during this time. Thus to a first order, precipitation efficiency can be evaluated from

$$\text{PE} - \frac{\text{HVF}_3}{\text{VVF}_2} + \frac{E_{\text{PBL}}}{\text{VVF}_2} \approx 1. \quad (6)$$

The model output does not enable a calculation of  $E_{\text{PBL}}$ , so it is estimated from (5) as the residual term in the water budget. The three ratios in (6) are shown in Table 3 during the period of precipitation over the CM. The approximate balance of (6) applies within  $\sim 20\%$ . During the shallow convective stage (2100 and 2200 UTC) the majority of the vapor advected into cloud base detrains laterally in the free troposphere ( $\text{HVF}_3 < 0$ ) or falls as rain but evaporates before reaching the ground ( $E_{\text{PBL}}$ ). As cumulus deepens over the CM from 2200 to 2300 UTC (Fig. 4a), most vapor (including the detrained cloud water) is advected away from the mountain, and the precipitation remains very limited; the PE does not exceed 1%. It is not until 0000 UTC, when most of

TABLE 3. Select water fluxes expressed as a percentage of the vertical vapor flux across the PBL top ( $\text{VVF}_2$ ) during the period of precipitation at the surface.

6 Aug 2006 water fluxes expressed as a percentage of $\text{VVF}_2$				
	Time (UTC)	$P_{\text{sfc}}$ (Precipitation efficiency)	$E_{\text{PBL}}$	$-\text{HVF}_3$
Shallow convection	2000	0	0	80
	2100	1	25	69
Deep convection	2200	0	13	86
	2300	1	17	81
	0000	42	47	11
	0100	10	38	52
Avg		9	23	63

precipitation occurs (Fig. 7c), that we see an increase in PE to 42%, but at this time rain is more likely to evaporate into the PBL (47%) than to reach the ground. On average, over the life cycle of this orographic convection episode, the PE is just 9% and the vapor outflux aloft ( $-\text{HVF}_3$ ) is 63%; thus, this convection effectively pumps BL water vapor into the free troposphere. We performed sensitivity studies with two other cloud microphysics parameterizations [the Eta scheme and the Thompson et al. (2008) scheme] and obtained similar results (PE values of 4% and 12%, respectively, over the duration of the simulated moist convection), notwithstanding substantially different storm evolutions.

These estimates of PE are low compared to that for high-plains thunderstorms [e.g., 55% according to Auer and Marwitz (1968) and 19%–47% according to Fankhauser (1988)]. However, a more thorough study of monsoon thunderstorms in China finds that over 90% of the water vapor that enters the clouds through the cloud base detrains in the ambient atmosphere and that less than 10% falls out as surface precipitation (Shusse and Tsuboki 2006). Clearly storm-total PE is a function of storm dimensions and surface dewpoint depression. The modeled PE cannot be verified because none of the 11 stations reported any precipitation on 6 August and the Tucson S-band radar echoes due to rain cannot be distinguished from ground clutter and biological return.

### 5. Discussion

An initial burst of Cu congestus growth occurs around local solar noon (1900–2000 UTC; Figs. 6d,e) in the WRF simulations for this case (6 August 2006). Since the level of free convection is well below the PBL top over the mountain at this time (Fig. 4a), this Cu development is due to local destabilization, with a CAPE value of  $260 \text{ J kg}^{-1}$  over the mountain (Fig. 4a), rather than being forced by upslope flow. Cloud shading and convective downdrafts of

lower  $\theta_e$  air suppress the solenoidal forcing (Fig. 6f) and MSC (Fig. 5c) around 2100 UTC. This is followed by a new cycle of warming of the CBL over the mountain, an increase in CAPE, and the growth of more numerous and deeper convective towers between 2200 and 0000 UTC, culminating in cumulonimbus formation (Figs. 4a and 7). During this period MSC in the CBL is enhanced to feed the growing convection (Fig. 5c), until convection matures and divergent cold pools form (Figs. 7 and 10).

This case study thus indicates that daytime orographic convection is initiated by local surface heating and destabilization rather than by upslope flow, which reduces CAPE over elevated terrain. A phase of suppressed MSC may increase chances for convective (re)initiation over a mountain. Boundary layer MSC may increase in response to the growth of sufficiently deep and large convection, before changing sign due to the decay of orographic convection. Thus, orographic convection differs from convection over flat land, in that the former is initiated by local heating and the latter by BL convergence (e.g., chapter 5 in Markowski and Richardson 2010). The collapse of convection produces a surface flow signal that is at least as apparent as its growth, consistent with Geerts et al. (2008) and Demko et al. (2009).

It is unlikely that convective conditioning of the environment [i.e., the moisture–convection feedback hypothesis; e.g., Derbyshire et al. (2004); Grabowski and Moncrieff (2004)] explains why the second burst of convection on 6 August is deeper and more intense than the first one. This hypothesis states that convective towers are more resistant to erosion by entrainment in an environment moistened by preceding towers. While moistening does occur in volume 3 (the Cu layer) during both convective bursts, the modeled BL  $\theta_e$  is higher at the start of the second burst (2200 UTC) than at the start of the first burst (1800 UTC, not shown), and CAPE is higher during the second burst than the first burst (Fig. 4a). Thus, changes in the BL are consistent with a relatively deeper second burst of orographic convection. Also, a lull of 1–2 h exists between the two bursts, which is long enough to advect the moisture in the Cu layer away from the mountain, notwithstanding the weak winds (Fig. 2). Moreover, at a resolution of 1 km, the WRF-resolved convective towers (e.g., Fig. 13) are unlikely to be much affected by entrainment, as discussed in section 2a.

## 6. Conclusions

This paper uses numerical model output to examine how the convective boundary layer over a mountain affects and is affected by locally triggered deep convection. It is based on a case study for a ~30-km-wide, ~2-km-high mountain, in an environment marked by weak winds,

weak wind shear, and modest CAPE. It builds on Part I, which uses WRF model output to examine CBL evolution over the same mountain for two other cases: one cloud-free and another with orographic Cu congestus.

Surface, upper-air, and photogrammetric data collected as part of CuPIDO indicate that the model, WRF v.3 with a horizontal resolution of 1- and 12-km NAM initial fields, reasonably captures the observed temperature distribution, as well as mountain-scale anabatic flow development, the CBL depth, and the stability and wind profiles. Convective growth is delayed a little in the model and the simulated maximum Cu top over the mountain is higher than observed, resulting in more precipitation than observed. These minor disagreements can be attributed at least in part to the absence (in the model) of a midlevel cap and a midlevel dry layer, and an underestimate in local soil moisture. These discrepancies would lessen if CuPIDO field data, such as soundings and surface measurements, had been assimilated into the WRF simulations.

The findings from the present case study corroborate several results in Part I, as follows:

- 1) Drainage flow transitions shortly after sunrise into anabatic, convergent flow, which peaks close to solar noon.
- 2) The anabatic flow is forced by a warm anomaly in the lower half of the CBL over the mountain, thus a horizontal pressure gradient force is directed towards the mountain. The low-level convergent flow advects cold air, but the resulting local cooling is offset by the sensible heat flux over the mountain surface.
- 3) The anabatic pressure gradient forcing persists for some time in the evening, even on a day with afternoon thunderstorms. This forcing results in highly convergent flow in the residual CBL above the drainage flow in a shallow stable layer.

The first two findings corroborate CuPIDO observations (Geerts et al. 2008; Demko et al. 2009). The following additional conclusions can be drawn from the present case study (6 August 2006):

- 4) In the absence of moist convection, the solenoidal circulation is largely contained within the CBL over the mountain, with low-level convergence and upper-level divergence. Deep convection converts this BL circulation into a tropospheric one, with inflow over the depth of the CBL, mainly the lower CBL, and outflow in the free troposphere aloft.
- 5) Orographic convection tends to be triggered along a convergence line, which arises from the solenoidal circulation but may drift downwind of the terrain crest. Such a boundary may be long lived and may be

the focus of further convective development as it intersects outflow boundaries or local terrain ridges.

- 6) Orographic convection is triggered by local destabilization rather than by anabatic flow, which lowers CAPE over the mountain as it advects colder air. Thus, a period of suppressed anabatic flow (e.g., following a first growth phase of orographic Cu convection) can be a precursor for renewed and possibly deeper Cu convection, as long as the surface heating remains intense. This may explain the cyclic nature of daytime convection over a mountain of this size (e.g., Zehnder et al. 2006).
- 7) Orographic convection in southeastern Arizona does not efficiently produce rain: over the lifetime of the convection, only about 10% of the vertical water vapor flux at cloud base precipitates on the ground. Instead, the “sky island” mountains are effective conduits of water vapor from the BL into the free atmosphere.

The ability of version 3 of the WRF model to capture the development of the CBL, the anabatic flow over steep terrain, and the timing and intensity of deep convection at a rather coarse spatial resolution is impressive. Thus, we can be optimistic that as the operational WRF model approaches a 1-km resolution in the near future, the predictability of orographic convection and convective precipitation in the western United States will improve substantially.

*Acknowledgments.* This research was funded by National Science Foundation (NSF) Grants ATM-0444254 and ATM-0849225 and by NSF facility deployment funds. The observed cloud-top chronology (shown in Fig. 4) was kindly provided by Joseph A. Zehnder.

#### REFERENCES

- Auer, A. H., and J. D. Marwitz, 1968: Estimates of air and moisture flux into hailstorms on the high plains. *J. Appl. Meteor.*, **7**, 196–198.
- Banta, R. M., 1984: Daytime boundary-layer evolution over mountainous terrain. Part I: Observations of the dry circulations. *Mon. Wea. Rev.*, **112**, 340–356.
- , and C. L. B. Schaaf, 1987: Thunderstorm genesis zones in the Colorado Rocky Mountains as determined by traceback of geosynchronous satellite images. *Mon. Wea. Rev.*, **115**, 463–476.
- Braham, R. R., 1952: The water and energy budgets of the thunderstorm and their relation to thunderstorm development. *J. Meteor.*, **9**, 227–242.
- Bright, D. R., and S. L. Mullen, 2002: Short-range ensemble forecasts of precipitation during the Southwest Monsoon. *Wea. Forecasting*, **17**, 1080–1100.
- Damiani, R., and Coauthors, 2008: Cumulus Photogrammetric, In-situ and Doppler Observations: The CuPIDO 2006 experiment. *Bull. Amer. Meteor. Soc.*, **89**, 57–73.
- Demko, J. C., and B. Geerts, 2010: A numerical study of the evolving convective boundary layer and orographic circulation around the Santa Catalina Mountains in Arizona. Part I: Circulation without deep convection. *Mon. Wea. Rev.*, **138**, 1902–1922.
- , —, Q. Miao, and J. Zehnder, 2009: Boundary-layer energy transport and cumulus development over a heated mountain: An observational study. *Mon. Wea. Rev.*, **137**, 447–468.
- Derbyshire, S. H., I. Beau, P. Bechtold, J.-Y. Grandpeix, J.-M. Piriou, and J.-L. Redelsperger, 2004: Sensitivity of moist convection to environmental humidity. *Quart. J. Roy. Meteor. Soc.*, **130**, 3055–3079.
- Ek, M. B., K. E. Mitchell, Y. Lin, E. Rogers, P. Grunmann, V. Koren, G. Gayno, and J. D. Tarpley, 2003: Implementation of Noah land surface model advances in the National Centers for Environmental Prediction operational mesoscale Eta model. *J. Geophys. Res.*, **108**, 8851, doi:10.1029/2002JD003296.
- Fankhauser, J., 1988: Estimates of thunderstorm precipitation efficiency from field measurements in CCOPE. *Mon. Wea. Rev.*, **116**, 663–684.
- Fuhrer, O., and C. Schär, 2005: Embedded cellular convection in moist flow past topography. *J. Atmos. Sci.*, **62**, 2810–2828.
- Geerts, B., Q. Miao, and J. C. Demko, 2008: Pressure perturbations and upslope flow over a heated, isolated mountain. *Mon. Wea. Rev.*, **136**, 4272–4288.
- Giorgi, F., 1991: Sensitivity of simulated summertime precipitation over the western United States to different physics parameterizations. *Mon. Wea. Rev.*, **119**, 2870–2888.
- Gochis, D. J., A. Jimenez, C. J. Watts, J. Garatuza-Payan, and W. J. Shuttleworth, 2004: Analysis of 2002 and 2003 warm-season precipitation from the North American Monsoon Experiment event rain gauge network. *Mon. Wea. Rev.*, **132**, 2938–2953.
- Grabowski, W. W., and M. W. Moncrieff, 2004: Moisture-convection feedback in the tropics. *Quart. J. Roy. Meteor. Soc.*, **130**, 3081–3104.
- Hobbs, P. V., T. J. Matejka, P. H. Herzegh, J. D. Locatelli, and R. A. Houze, 1980: The mesoscale and microscale structure and organization of clouds and precipitation in midlatitude cyclones. I: A case study of a cold front. *J. Atmos. Sci.*, **37**, 568–596.
- Hohenegger, C., and C. Schär, 2007: Atmospheric predictability at synoptic versus cloud resolving scales. *Bull. Amer. Meteor. Soc.*, **88**, 1783–1793.
- Janjić, Z. I., 1996: The Mellor–Yamada level 2.5 turbulence closure scheme in the NCEP Eta Model. Research Activities in Atmospheric and Oceanic Modeling, WMO, CAS/JSC WGNE, Geneva, Switzerland, 4.14–4.15. [Available from World Meteorological Organization, Case Postale 2300, CH-1211 Geneva, Switzerland.]
- Jiang, Q., and R. B. Smith, 2003: Cloud timescales and orographic precipitation. *J. Atmos. Sci.*, **60**, 1543–1559.
- Li, J., X. Gao, R. A. Maddox, and S. Sorooshian, 2004: Model study of evolution and diurnal variations of rainfall in the North American Monsoon during June and July 2002. *Mon. Wea. Rev.*, **132**, 2895–2915.
- Lin, Y. L., R. D. Farley, and H. D. Orville, 1983: Bulk parameterization of the snow field in a cloud model. *J. Climate Appl. Meteor.*, **22**, 1065–1092.
- Markowski, P. M., and Y. P. Richardson, 2010: *Mesoscale Meteorology in Midlatitudes*. Wiley, 430 pp.
- McCollum, D. M., R. A. Maddox, and K. W. Howard, 1995: Case study of a severe mesoscale convective system in Central Arizona. *Wea. Forecasting*, **10**, 643–665.
- Shusse, Y., and K. Tsuboki, 2006: Dimension characteristics and precipitation efficiency of cumulonimbus clouds in the region

- far south from the Mei-Yu front over the eastern Asian continent. *Mon. Wea. Rev.*, **134**, 1942–1953.
- Skamarock, W. C., and Coauthors, 2008: A description of the Advanced Research WRF Version 3. NCAR Tech. Note NCAR/TN-475+STR, 125 pp. [Available online at [http://www.mmm.ucar.edu/wrf/users/docs/arw\\_v3.pdf](http://www.mmm.ucar.edu/wrf/users/docs/arw_v3.pdf).]
- Thompson, G., P. R. Field, W. R. Hall, and R. M. Rasmussen, 2008: Explicit forecasts of winter precipitation using an improved bulk microphysics scheme. Part II: Implementation of a new snow parameterization. *Mon. Wea. Rev.*, **136**, 5095–5115.
- Walser, A., and C. Schär, 2004: Convection-resolving precipitation forecasting and its predictability in Alpine river catchments. *J. Hydrol.*, **288**, 57–73.
- Wandishin, M. S., D. J. Stensrud, S. L. Mullen, and L. J. Wicker, 2008: On the predictability of mesoscale convective systems: Two-dimensional simulations. *Wea. Forecasting*, **23**, 773–785.
- Yuan, H., S. L. Mullen, X. Gao, S. Sorooshian, J. Du, and H. M. H. Juang, 2007: Short-range probabilistic quantitative precipitation forecasts over the Southwest United States by the RSM Ensemble System. *Mon. Wea. Rev.*, **135**, 1685–1698.
- Zehnder, J. A., L. Zhang, D. Hansford, A. Radzan, N. Selover, and C. M. Brown, 2006: Using digital cloud photogrammetry to characterize the onset and transition from shallow to deep convection over orography. *Mon. Wea. Rev.*, **134**, 2527–2546.
- , J. Hu, and A. Razdan, 2007: A stereo photogrammetric technique applied to orographic convection. *Mon. Wea. Rev.*, **135**, 2265–2277.